Soft Matter

COMMUNICATION

View Article Online
View Journal | View Issue

Cite this: *Soft Matter*, 2025, 21, 8323

Received 2nd September 2025,
Accepted 13th October 2025

DOI: 10.1039/d5sm00892a

rsc.li/soft-matter-journal

Effect of the pH value on compression and array structures of highly charged microgels at the air/water interface

Takahisa Kawamoto, Haruka Minato * and Daisuke Suzuki *

Understanding the interfacial behavior of stimuli-responsive microgels is critical for applications such as foam and emulsion stabilization, as well as for the fabrication of two-dimensional colloidal crystals using the interfaces. In this study, the pH-dependent compression behavior and array structures of micron-sized poly(*N*-isopropylacrylamide-*co*-acrylic acid) microgels at the air/water interface was investigated. By combining a Langmuir trough with fluorescence microscopy, microgel arrays under compression and acidic (pH = 3) or basic (pH = 9) conditions were directly visualized. At pH = 9, the carboxyl groups within the microgels are deprotonated, resulting in significant swelling and the formation of ordered hexagonal arrays with high crystallinity ($\Psi_6 > 0.84$) upon compression. In contrast, at pH = 3, the carboxyl groups within the microgels are protonated, leading to a suppression of the electrostatic repulsion between neighboring microgels and a reduction in crystallinity ($\Psi_6 \sim 0.70$) of the microgel arrays before and after compression. Furthermore, the calculated surface-compression modulus using the compression isotherms indicated higher interfacial elasticity for charged microgels, demonstrating that electrostatic repulsion governs both array ordering and mechanical robustness. These findings provide fundamental insights into the role of charge in controlling the microgel structure and mechanics at interfaces, thus offering further guidelines for the design of stimuli-responsive materials and stabilizers for foams and emulsions.

Introduction

Hydrogel microspheres (microgels) are soft colloidal particles that contain >90% water, a feature that endows them with high deformability[1–6] compared to conventional rigid particles made from *e.g.*, polystyrene or silica. Moreover, microgels can respond to external stimuli, such as changes in temperature and pH value, which can reversibly change their physicochemical properties.[1–6] Therefore, microgels have found applications in a wide range of fields, including chemical/biological separations,[7–12] switchable catalysts,[13–16] colloidal crystals/glasses,[17–22] biomedical materials,[23,24] autonomous actuators,[25–29] and particulate stabilizers.[30–33]

Furthermore, soft microgels have been widely recognized for their unique behavior patterns at fluid interfaces, specifically at air/water[34–38] and oil/water interfaces.[36–38] For instance, microgels composed of poly(*N*-isopropylacrylamide) (pNIPAm),[39,40] a common thermo-responsive polymer, exhibit surface activity, undergo significant deformation immediately upon adsorption at the air/water interface and can reduce interfacial tension.[41,42] Therefore, microgels at such interfaces have been the subject of prolonged significant attention, particularly with respect to potential applications as stabilizers for foams[31,33] and emulsions.[30,32]

To obtain uniformly sized pNIPAm-based microgels, microgels are usually synthesized *via* precipitation polymerization. In this method, the commonly used crosslinker *N*,*N*′-methylenebis-(acrylamide) (BIS) exhibits a higher reactivity ratio than the main monomer *N*-isopropylacrylamide (NIPAm). Therefore, BIS is consumed preferentially during the early stages of polymerization, leading to the formation of microgels with a heterogeneous crosslinking density, *i.e.*, a densely crosslinked core surrounded by a loosely crosslinked shell.[1–6] This structural heterogeneity is preserved even after adsorption to interfaces, resulting in a "fried-egg"-like morphology at the interface. The extent of deformation at the interface depends on both the internal architecture of the microgels and the nature of the fluid phases. Differences in the structure of microgels, *e.g.*, the core–shell ratio, lead in turn to changes of the compression behavior of the microgels at the interface.[34–36]

Although numerous studies have investigated the stimuli-responsive behavior of microgels in bulk dispersions, their responsiveness at fluid interfaces remains less well understood. Interestingly, it has been reported that microgels adsorbed at the air/water interface show minimal change in lateral dimension or protrusion height upon variation of temperature or pH value, suggesting that the in-plane structure of microgels is

Graduate School of Environmental, Life, Natural Science and Technology, Okayama University, 3-1-1 Tsushimanaka, Kita-ku, Okayama, 700-8530, Japan.
E-mail: h_minato@okayama-u.ac.jp, d_suzuki@okayama-u.ac.jp

retained due to strong adsorption to the interface.[34–38] These findings underscore the complex compression behavior of soft microgels, which is distinct from that of rigid particles, and highlight the importance of understanding how their interfacial structures and properties are governed by the surrounding environment.[43–50] Nevertheless, direct observation of individual microgels and their array structures under compression remains challenging due to optical-resolution limits associated with submicron particle sizes and low polymer density.[51,52] To the best of our knowledge, there have been no previous studies that report on the direct visualization and analysis of the structure of microgels adsorbed on the air/water interface upon compression under different pH environments.

In addition, the mechanical responses of microgel monolayers, such as their interfacial compression modulus and elasticity, have been actively investigated. Previous studies have reported that the interfacial elasticity is strongly influenced by several factors, including charge density,[53,54] crosslinking density,[55,56] packing density,[57] and interparticle interaction potentials of microgels,[58] and ionic strength and pH.[59] These studies have demonstrated that microgel deformability influences the interfacial mechanics. However, the combined effect of pH-induced charge modulation and microgel deformation on the interfacial elasticity has not yet been fully clarified.

Against this background, our group has investigated the self-organization of microgels and soft deformable particles during the evaporation of sessile droplets.[60–66] Microgels spontaneously adsorb and gradually order themselves at the air/water interface of diluted dispersions, resulting in a reduction in the distance between their centers due to the decrease in interfacial area.[60] Moreover, the ordered structure of a microgel monolayer formed at the air/water interface remains intact on solid substrates after evaporation. The effects of microgel size, shape, crosslinking density, chemical species, and charge density on this self-organization have been examined.[62,63] A series of studies revealed that microgel arrays at the air/water interface and on solid substrates are not always the same after drying sessile droplets and whether the ordered structures formed at fluid interfaces are preserved on a solid substrate depends on the properties of the microgels.[63,67] In particular, the array structures of polyacrylamide-based microgels and highly charged poly (NIPAm-*co*-acrylic acid (AAc)) microgels, while forming ordered structures at the air/water interface, become disordered due to capillary forces during water evaporation.[63] This behavior is similar to that of rigid colloidal particles made of *e.g.*, polystyrene. Therefore, the direct visualization of microgels adsorbed at interfaces is important in order to understand the relationship between the structures and properties (or functions) of microgel/microgel arrays.[67] Recently, the compression behavior of microgels at the air/water interface has been successfully visualized and quantified by combining a Langmuir trough with a fluorescence-microscopy system.[68–70] By employing relatively large microgels ($\sim$4 μm in diameter at the interface) synthesized *via* a modified precipitation-polymerization method, we were able to directly observe and analyze both individual shapes and array structures of microgels during compression. Furthermore, we could correlate their structural changes with the π–A isotherm, revealing that not only the arrangement of microgel arrays but also the deformation of individual microgels contributes to the compression modulus of microgel arrays, emphasizing the importance of understanding their interfacial behavior from multiple perspectives.[70]

Furthermore, we found that differences in the pH value of aqueous media has a significant impact on the compression behavior and interfacial arrangement of adsorbed poly(NIPAm-*co*-AAc) microgels at the air/water interface. The pH-dependent interfacial behavior of microgels has garnered growing attention due to their potential application as responsive stabilizers for foams and emulsions. Unlike rigid colloidal particles, whose interfacial behavior is dominated by long-range electrostatic repulsion, previous studies have suggested that, for soft microgels, the observed changes under different pH conditions arise primarily from pH-induced differences in swelling behavior rather than from direct electrostatic interactions.[54] In this study, in order to gain deeper insights into the compression behavior of stimuli-responsive microgels, we employed micrometer-sized poly(NIPAm-*co*-AAc) microgels that were designed to exhibit pronounced pH responsiveness by incorporating a high density of charged monomers, while also being suitable for a direct visualization at the air/water interface. The compression behavior was investigated through a simultaneous monitoring of the surface pressure and a direct visualization of the microgels for both protonated and deprotonated states of the acrylic-acid moieties.

Experimental

Materials

N-Isopropyl acrylamide (NIPAm, 98%), *N*,*N*′-methylenebis(acrylamide) (BIS, 97%), potassium peroxodisulfate (KPS, 95%), potassium chloride (KCl, 99.5%), disodium hydrogen phosphate (Na_2HPO_4, 99.5%), anhydrous sodium dihydrogen phosphate (KH_2PO_4, 99%), 1-ethyl-3-(3-dimethylaminopropyl)-carbodiimide hydrochloride (EDC·HCl, 98%), sodium chloride (NaCl, 99%), hydroxide solution (NaOHaq.), hydrochloric acid solution (HClaq.), methanol (MeOH, 99.8%), and ethanol (EtOH, 99.5%) were purchased from FUJIFILM Wako Pure Chemical Corporation (Japan) and used as received. Acrylic acid (AAc, 99%) was purchased from Sigma-Aldrich and used as received. 5-Aminofluorescein (isomer I) was purchased from TCI (Japan) and used as received. Deionized water was prepared using an EYELA, SA-2100E1 (Japan) automatic water-distillation apparatus prior to use.

Microgel synthesis

The synthesis of the micron-sized microgels is described in detail in a previous study.[70] In a nutshell, the micron-sized microgels were synthesized *via* a modified aqueous free-radical precipitation polymerization. For that purpose, a monomer solution (NIPAm: 0.9505 g; AAc: 0.1081 g; BIS: 0.0154 g; water: 99 mL) was heated to 40 °C with stirring at 250 rpm in a four-necked round-bottom flask (300 mL). After deoxygenating the solution with nitrogen gas for 30 minutes, the initiator (KPS,

0.055 g in 1 mL of water) was added. Then, the temperature was raised from 40 °C to 60 °C (1 °C/3 min). When the polymerization temperature reached 60 °C after 1 h, another monomer solution (NIPAm: 5.038 g; AAc: 1.405 g; BIS: 0.1503 g; NaCl: 0.0380 g) was added at 200 μL min^{-1} using a syringe pump. After 5 hours, the feed was stopped and the solution was stirred at 60 °C for 2 more hours, before the dispersion was cooled to room temperature to stop the polymerization. The microgel dispersion was centrifuged and redispersed twice at 50 000 G, followed by dialysis against pure water for a week.

Microgel labelling

To visualize the microgels using fluorescence microscopy, a fluorescent dye, 5-aminofluorescein (isomer I) was chemically attached to the carboxyl groups derived from AAc within the microgels *via* a carbodiimide reaction.[68,70] Initially, the microgels were dispersed in a phosphate-buffered saline (PBS) solution composed of 137 mM NaCl, 2.68 mM KCl, 2 mM KH_2PO_4, and 10 mM Na_2HPO_4, and the pH value was adjusted to 7.4 using an aqueous HCl solution. Subsequently, 5-aminofluoresane (0.2605 g) and water-soluble carbodiimide (0.1438 g; EDC) were added in proportions corresponding to a 1 molar fraction of the carboxyl groups present in the dispersion. The mixture was stirred using a magnetic stirrer under shaded conditions for approximately 18 h. Then, the reaction solution was purified three times *via* centrifugation and redispersion with methanol to eliminate any unreacted fluorescent dye, using an RCF of 70 000 g. This was followed by five washes with pure water to replace the remaining solvent.

Characterization by optical/fluorescence microscopy

The intrinsic viscosity [η] of the microgels at 25 °C was evaluated based on the viscosity of diluted dispersions measured with an Ubbelohde viscometer.[71] As is customary when dealing with microgels, the apparent volume fraction of the microgels (Φ_{eff}; $\Phi_{eff} = c[\eta]/2.5$) was employed as a simple measure of the degree of packing. The critical concentration (C^*) is the concentration where $\Phi_{eff} = 1$. The microgels were transferred into rectangular Vitrotube borosilicate capillaries (0.1 mm × 2.0 mm) by capillary force. The diameters of the microgels were measured using optical/fluorescence microscopy (BX53, Olympus) to quantify the center-to-center distance between the microgels packed at C^*. This characterization was performed similarly at different pH values (pH = 3 or 9).

Characterization of the microgel surface using electrophoresis

The electrophoretic mobility (μ) of each individual microgel was measured by electrophoretic light scattering (ELS) using a Zetasizer NanoZS (Malvern). Dilute dispersions, whose ionic strength was adjusted using NaCl, were equilibrated at the target temperature for 10 minutes. The μ value was measured under an applied potential of 40 V using the laser Doppler method (scattering angle: 173°), averaging 20 independent measurements. This process was repeated three times for improved data reliability. The same evaluation was performed at different pH values (pH = 3 or 9), whereby the ionic strength was standardized to 1 mM using NaCl.

Characterization of the microgels compressed at the air/water interface

Compression isotherms at the air/water interface were evaluated using a Langmuir trough (dimensions: 140 mm × 680 mm; compressible area: 924 cm^2; Kyowa Interface Science Co., Ltd) equipped with a Wilhelmy plate, a chiller set to 25 °C, and a fluorescence-microscopy system (lamp: HBO-100; excitation: 450–490 nm; emission: 510 nm; Axio Scope.A1, Zeiss). Images and videos of the compressed microgels were captured using a CCD camera (Image X Earth Type S-2.0M Ver. 3.1.3, Kikuchi Optical Co., Ltd). The surface pressure (π in mN m^{-1}) at the air/water interface was measured using the Wilhelmy method. First, a blank measurement was conducted by filling the trough with water adjusted to each pH condition with an ionic strength of 1 mM. Microgels dispersed in a mixture of water and ethanol (1 : 1, v/v) were then spread over the entire air/water interface using a micropipette. After allowing 30 minutes for equilibration, the compression-isotherm evaluation began by moving the trough barrier at a constant speed of 10 cm^2 min^{-1} while directly observing the microgels at the air/water interface. Simultaneously, a dipper holding a glass substrate (Neo Micro Cover Glass, Matsunami Glass Ind., Ltd) was raised at a speed of 1 cm^2 min^{-1} at a vertical angle to transfer the microgel arrays formed at the interface onto the glass substrates. The compression modulus was calculated using the following eqn (1).

$$E_G = -(d\pi/d \ln A^*) \quad (1)$$

In this equation, A^* is the normalized area, *i.e.*, the interfacial area (m^2)/divided by the amount of added microgel (g). The parameter represents the surface elasticity of the particle layer.[72,73]

Image analysis

To analyze the microscopy images of the microgels, ImageJ (Version 2.0.0) and Python were used to determine the array structures and shapes. The hexagonal-order parameter (Ψ_6) was calculated using the following eqn (2).

$$\Psi_6 = \frac{1}{6}\sum_{j=1}^{6} \exp(6i\theta j) \quad (2)$$

In this equation, θj is the angle between adjacent microgels and i denotes the imaginary unit ($i^2 = -1$). A value of Ψ_6 close to 1 indicates an ideal hexagonal structure of microgels at the air/water interface.[74]

The shape of the microgels was evaluated using the circularity value, which is defined by the following eqn (3).

$$\text{Circularity} = (4\pi \cdot \text{Area})/(\text{Perimeter})^2 \quad (3)$$

Thus, a circularity value close to 1 indicates a shape that is close to circular.

Results and discussion

In this study, we employed micron-sized poly(NIPAm-*co*-AAc) microgels that we have previously developed and reported.[70]

These microgels were selected to enable the direct visualization at the air/water interface. Their low crosslinker content (BIS: 1 mol%) allows substantial deformation at the interface, facilitating direct observation, while their high acrylic-acid content (30 mol%) is expected to confer pronounced pH-responsiveness.[70] The acrylic-acid moiety is protonated at pH = 3 and deprotonated at pH = 9, and accordingly, charges in the microgels are introduced at high pH values. This is reflected in an increase in the electrophoretic mobility from -0.64×10^{-8} $m^2 V^{-1} s^{-1}$ at pH = 3 to -3.20×10^{-8} $m^2 V^{-1} s^{-1}$ at pH = 9. Moreover, this induces microgel swelling due to osmotic pressure from counterions. The size of the microgels increases from $D_{\Phi_{eff}=1} = 3.4 \pm 0.3$ μm (CV 8.9%) at pH = 3 to $D_{\Phi_{eff}=1} = 5.7 \pm 0.5$ μm (CV 7.9%) at pH = 9 (Fig. 1) in a three-dimensional packed state at the critical concentration (C^*; $\Phi_{eff} = 1$). These results confirm that the micron-sized microgels exhibit clear pH-responsiveness. In addition, these microgels were confirmed to have a core–shell structure, wherein the core has a higher polymer density on glass substrates.[70]

Firstly, the compression isotherms and the array structure of microgels at pH = 3 was investigated (Fig. 2). The shape of the π–A isotherm is similar to that obtained for comparable pNIPAm-based microgels at the air/water interface.[53,73] Moreover, we found that after spreading the microgels on the air/water interface, the microgel arrays formed inhomogeneous structures with numerous voids (approximately several tens of micrometers in diameter). Even after compression by barrier movement, the uniformity of the microgel arrays was not improved.

On the other hand, at pH = 9, highly ordered microgel arrays were formed over a wide area (Fig. 3). The obtained π–A isotherms under subphase pH = 9 did not exhibit a two-step increase observed at pH = 3, and π increased sharply, eventually reaching a plateau at ~34 mN m^{-1}. At the interface, the microgel arrays formed a highly ordered structure over a wide area with fewer voids even before compression, which stands in sharp contrast to the structure observed at pH = 3. This difference can be attributed to the increased surface-charge density of the microgels at pH = 9 that results in stronger electrostatic repulsion between microgels, which promotes the formation of highly ordered structures. Although ethanol was introduced during spreading on the air/water interface, causing some microgel shrinkage and suppression of steric repulsion, the electrostatic repulsion remained dominant at pH = 9 and may be responsible for the consistently high colloidal crystallinity across the entire interface. Although some colloidal crystal-grain boundaries were present (Fig. S2), these disappeared upon further compression. Moreover, in the

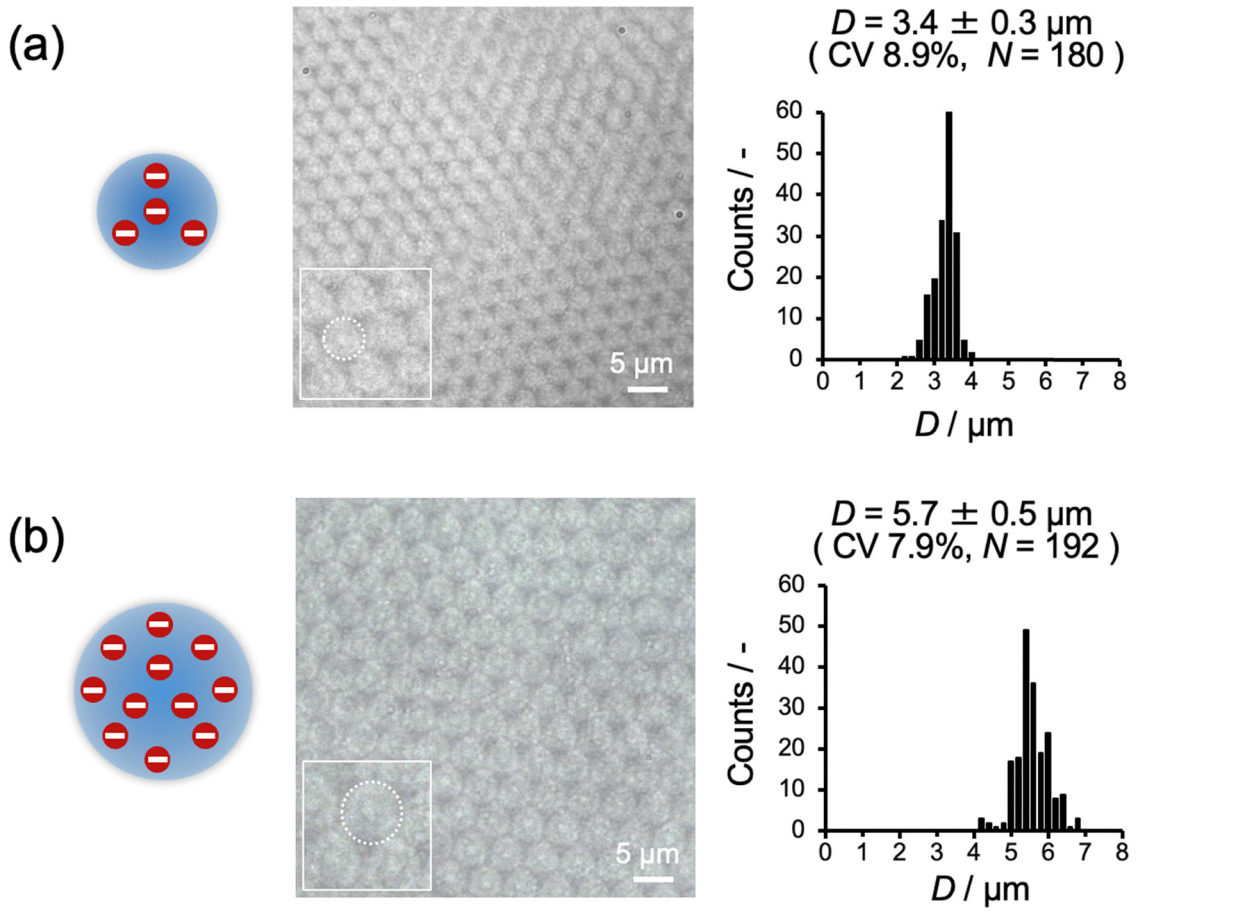

Fig. 1 Optical-microscopy images of colloidal crystals of the labelled micron-sized microgels at the critical concentration, C^*, at (a) pH = 3 and (b) pH = 9. The white dotted lines indicate individual microgels, together with histograms showing the size and size distribution of the microgels at each pH value.

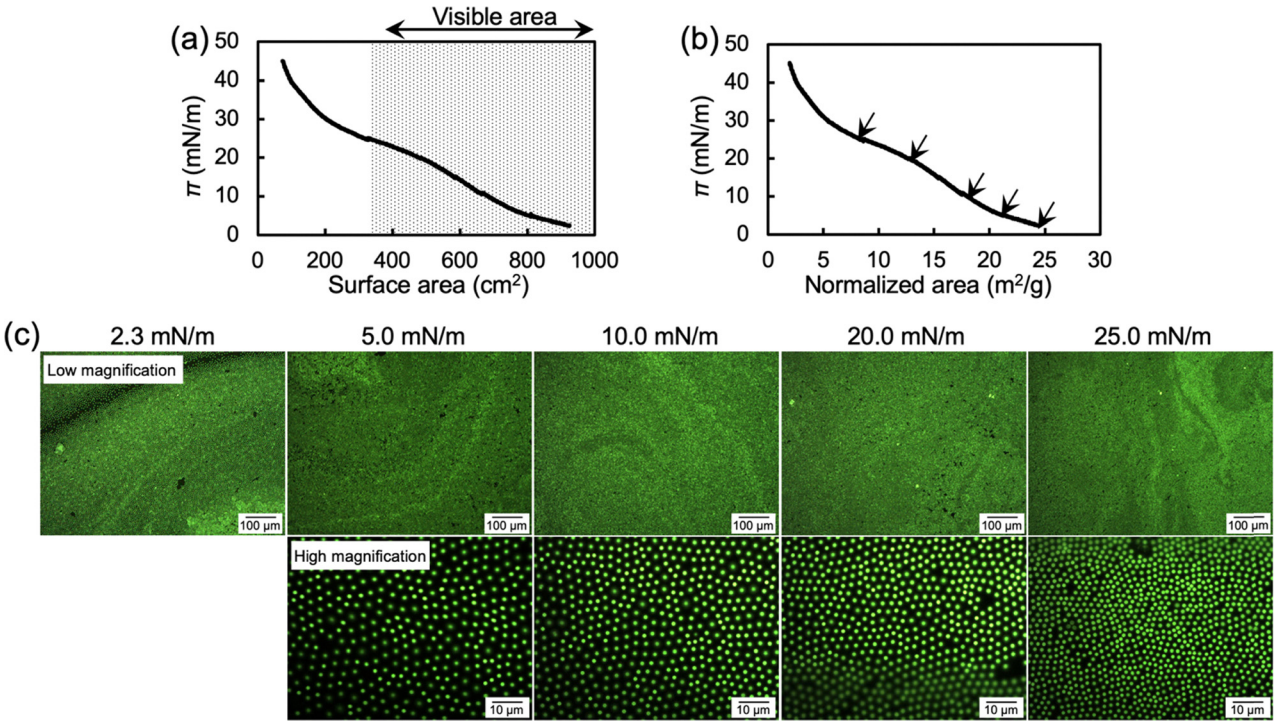

Fig. 2 (a) Surface pressure, π, *versus* surface area and (b) π *versus* normalized area (the interfacial area (m^2)/the amount of added microgel (g)) compression isotherms for the microgels at the air/water interface at pH = 3. The dotted area in (a) shows the range in which the microgels can be visualized using a fluorescence microscope during compression. (c) Representative fluorescence-microscopy images of the microgel arrays at the air/water interface at pH = 3 during compression when 3.8 mg of microgels were added. These images were obtained with a low-magnification and high-magnification lens. All high-magnification images are shown in Fig. S1.

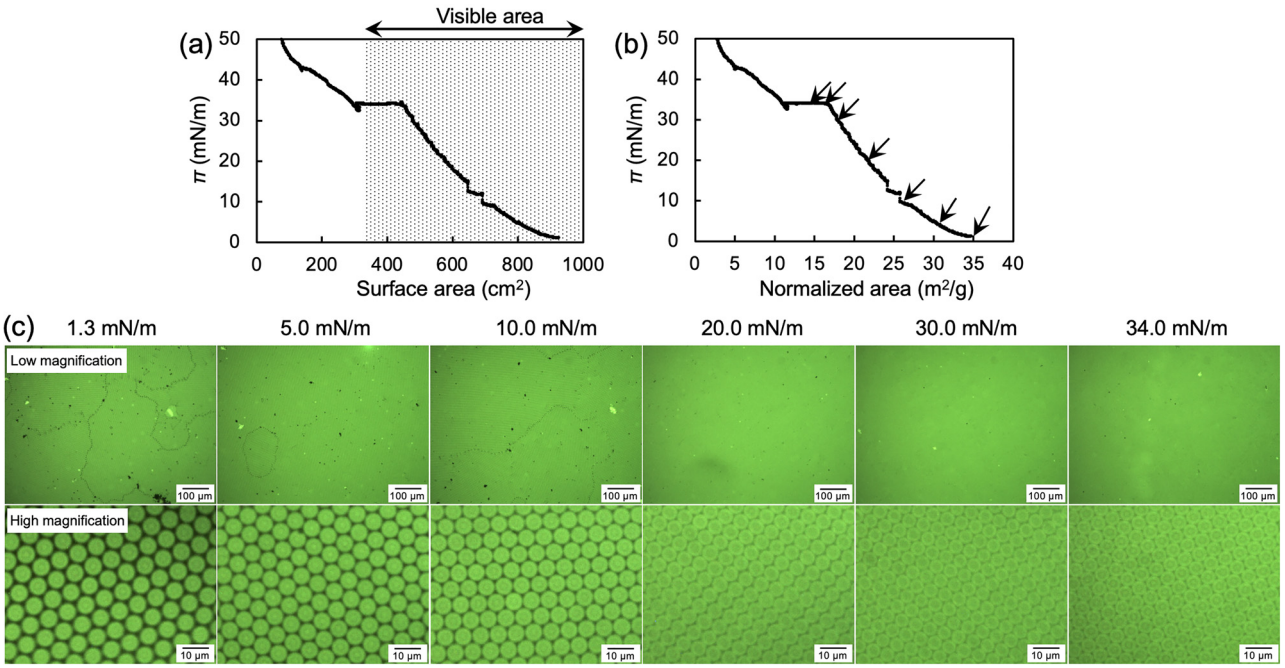

Fig. 3 (a) Surface pressure, π, *versus* surface area and (b) π *versus* normalized area (the interfacial area (m^2)/the amount of added microgel (g)) compression isotherms for the microgels at the air/water interface at pH = 9. The dotted area shows the range in which the microgels can be visualized using a fluorescence microscope during compression. (c) Representative fluorescence-microscopy images of the microgel arrays at the air/water interface at pH = 9 during compression when 3.2 mg of microgels were added. These images were obtained with a low-magnification and high-magnification lens. All high-magnification images are shown in Fig. S2.

region where the π–A isotherm reaches a plateau (~34.0 mN m^{-1}), the microgel arrays collapsed (Fig. S3). The observed re-increase of π in the higher compression region (surface area < 300 cm^2) is likely due to the extreme proximity of the Wilhelmy plate and the barrier.

We hypothesized at this point that highly ordered microgel arrays could potentially be obtained at low pH values once highly ordered microgels arrays have been formed at pH = 9. To confirm this hypothesis, microgels were initially spread at pH = 9, before the subphase was immediately adjusted to pH = 3 by adding HCl aq. to reach an ionic strength of 1 mM. Consequently, without compression, the microgel arrays were unable to maintain their ordered structures (Fig. S4). In contrast, once microgel arrays were first slightly compressed at pH = 9 (until π = 3 mN m^{-1}) before changing the subphase to pH = 3, the highly ordered structures were maintained. (Fig. 4) This behavior suggests that complete coverage of the interface by microgels restricts microgel mobility, and that the slight lateral compression promotes entanglement of polymer chains between neighboring microgels. In fact, the nearest-neighbor distance (D_{NND}) between microgels remained nearly unchanged when the subphase pH was changed from 9 to 3 (Fig. 5b; 5.5 μm at pH = 9 at 3 mN m^{-1}; 5.6 μm at pH = 3 at 3 mN m^{-1}).

Next, the hexagonal-order parameter Ψ_6 was analyzed to quantitatively evaluate the crystallinity of the microgel arrays. As shown in Fig. 5a, at pH = 9 for the subphase, the Ψ_6 value remained >0.84 regardless of surface pressure, indicating that the microgel arrays exhibit high colloidal crystallinity (Fig. 5a). For image analysis, fluorescence-microscopy images with medium-magnification lens, capable of identifying individual microgels and visualizing a large area, were selected (Fig. S2 and S5). It is important to note that microgels adjacent to voids were excluded from the analysis. In contrast, at pH = 3 for the subphase, the Ψ_6 value remained ~0.78 at low surface pressures ($3 \leq \pi \leq 20$ mN m^{-1}) and gradually decreased to ~0.70 after further compression ($20 \leq \pi \leq 23$ mN m^{-1}), which is most likely due to the appearance of polygonal array structures, such as hexagonal, rhombic, and square-like arrangements. It should also be noted here that the nearest-neighbor particle distance (D_{NND}) decreased monotonically with compression at pH = 3 and 9 (Fig. 5b), *i.e.*, from 5.5 μm to 4.0 μm at pH = 9 (0 to 33 mN m^{-1}) and from 5.6 μm to 4.5 μm at pH = 3 (3 to 20 mN m^{-1}).

We have previously investigated the crystallinity of microgel arrays synthesized from the same batch under pure-water conditions (pH ≈ 7).[70] At lower surface pressures (π < 25 mN m^{-1}), the microgel arrays exhibit high crystallinity, while at higher

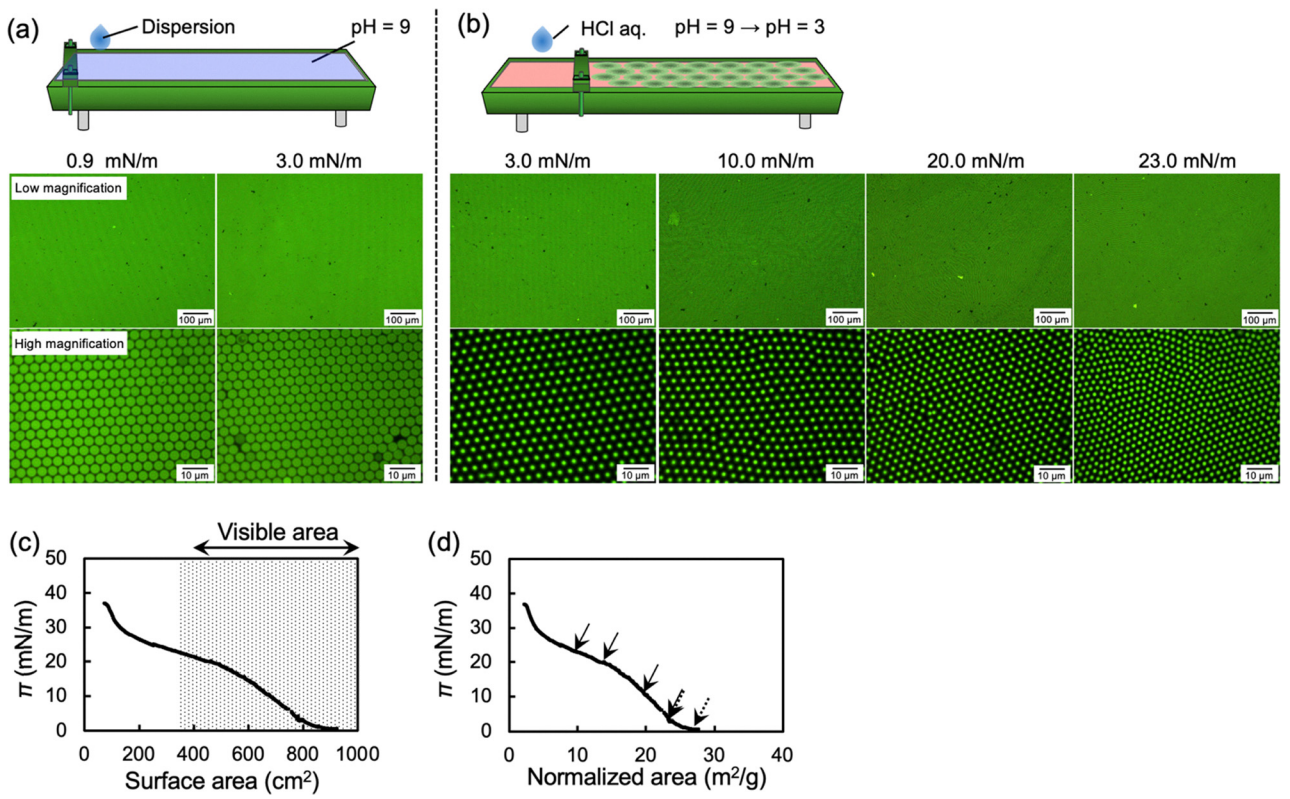

Fig. 4 Schematic illustration of LB trough experiments and representative fluorescence-microscopy images of the microgel arrays at the air/water interface during compression when 3.2 mg of microgels were added. (a) The dispersion was dropped on the interface whose pH value had been pre-adjusted to 9, before the microgel arrays were compressed to 3 mN m^{-1}. (b) The subphase pH was changed from pH = 9 to pH = 3 by adding HClaq. at 3 mN m^{-1}. (c) Surface pressure, π, *versus* surface area and (d) π *versus* normalized area (the interfacial area (m^2)/the amount of added microgel (g)) compression isotherms for the microgels at the air/water interface at pH = 9. The dotted area shows the range in which the microgels can be visualized using a fluorescence microscope during compression. All high-magnification images are shown in Fig. S4.

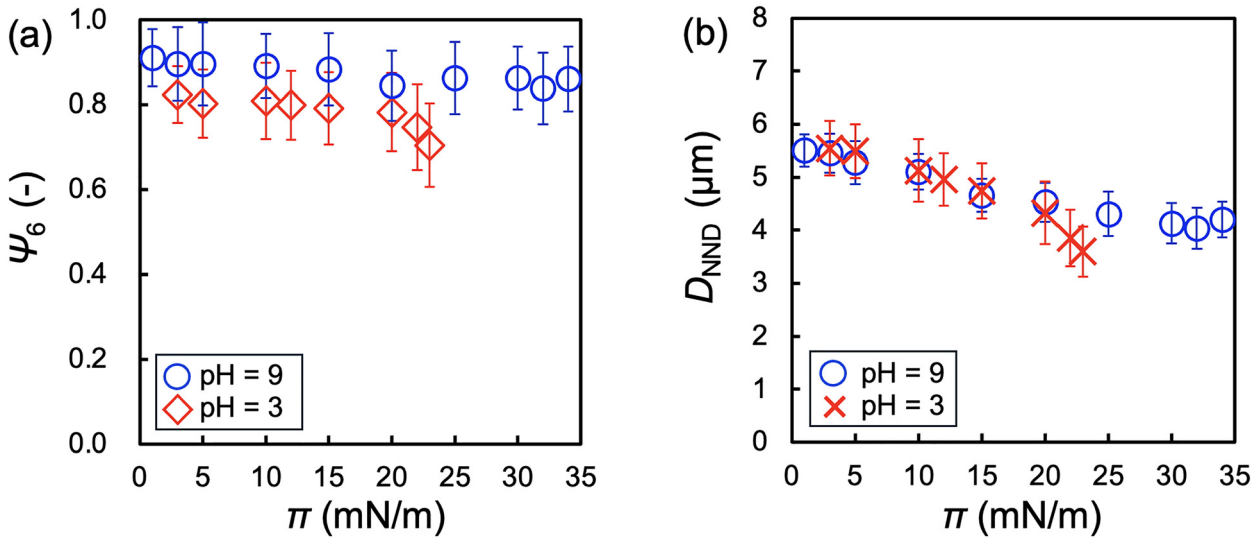

Fig. 5 (a) Hexagonal-order parameter, Ψ_6, and (b) the nearest-neighbor distances, D_{NND}, calculated from the fluorescence-microscopy images of the microgels adsorbed at the air/water interface (Fig. 3, 4 and Fig. S2, S4), as a function of π. It should be noted here that Ψ_6 was analyzed by excluding those microgels that neighbor voids or that are at the edge of the images to focus on the structural arrangement of neighboring microgels.

surface pressures ($\pi \geq 25$ mN m^{-1}), the Ψ_6 values gradually decrease, likely due to overlapping and deformable shell layers of the core–shell microgels, which allow slight interpenetration and suppress a rearrangement of the microgels at the interface.[70] Compared to our previous results, at pH = 9, the microgels carry a higher surface charge due to more deprotonation of the acrylic-acid groups, resulting in stronger electrostatic repulsion. Thus, it is plausible that the enhanced repulsion suppresses interpenetration of the shell layers and facilitates microgel rearrangement, thereby maintaining high colloidal crystallinity even upon compression. Different from the microgels where acrylic acid is deprotonated, as judging from the result obtained at pH = 3, weakly charged microgels are not arranged at the air/water interface before compression. Furthermore, the arranged structures as shown in Fig. 4b are disordered upon compression, which suggests that the shell layers of neighboring microgels can easily interpenetrate and that stronger attractive interparticle forces exist.

In order to evaluate not only the arrangement of microgels but also the shape of individual microgels under different pH conditions, non-labeled microgels were mixed with fluorescently labeled microgels to evaluate the structure of single microgels (Fig. 6 and Fig. S7). The fluorescence-microscopy images of the mixture revealed the shape of each labeled microgel at the

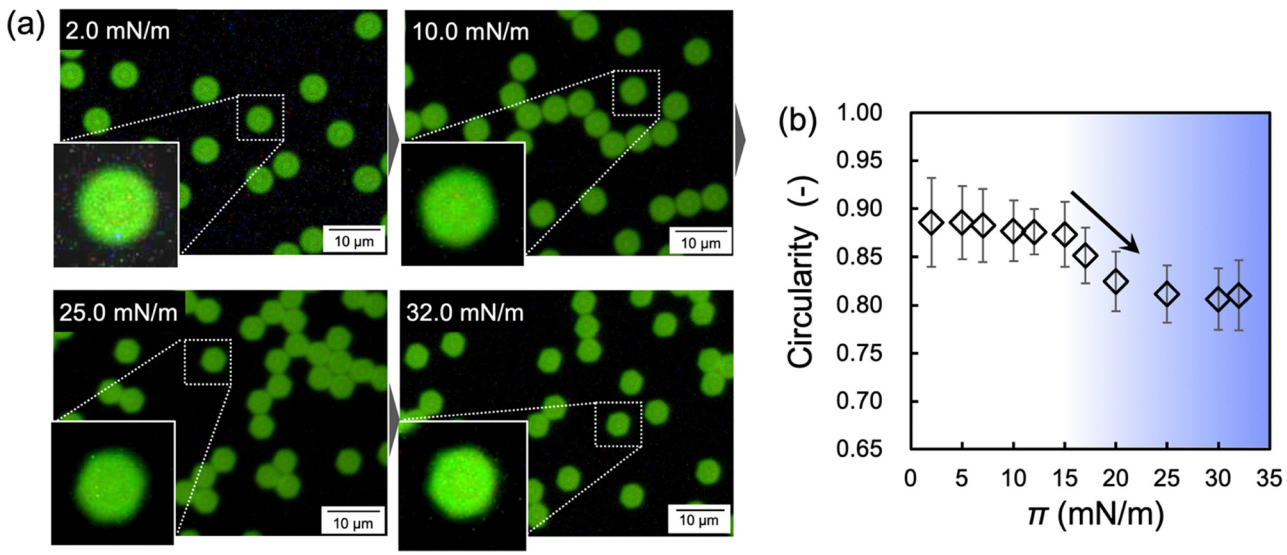

Fig. 6 (a) Fluorescence-microscopy images of the mixture of labelled and non-labelled microgels at the air/water interface during compression at pH = 9. These pictures were obtained with a high-magnification lens and trimmed. The full series of images at each π value is shown in Fig. S6 and S7. (b) Correlation between the circularity of the microgels and the surface pressure at pH = 9.

interface, as the non-labeled microgels, which are invisible, allowed for a clear visualization of the labeled ones (Fig. 6). The shape changes of the compressed microgels were quantitatively calculated using the circularity parameter, where a value close to 1 indicates a shape close to a perfect circle. At pH = 9, the circularity parameter remained ~0.9 until the surface pressure (π) reached 15 mN m^{-1}, indicating near-circular shapes. As the surface pressure increased further, the circularity parameter gradually decreased, eventually plateauing at ~0.80 ($20 \leq \pi \leq 34$ mN m^{-1}) (Fig. 6b). In contrast, at pH = 3, noticeable deformation of the microgels was not observed, not even at high π values, and the circularity parameter remained at ~0.90 (Fig. S6 and S8). It should also be noted here that the circularity-parameter results likely include deformation of the invisible outer shell during compression, which is beyond the detection limit of the fluorescence-microscopy measurements.

Finally, we conducted a detailed investigation into the correlation between structural changes in pH-responsive microgel arrays and their interfacial-surface properties. To gain further insight into the interfacial properties, the surface elasticity related to the compression modulus, $E_G = -d\pi/d \ln A^*$, was calculated, where A^* represents the particle-specific area per weight (Fig. 7). E_G is considered one of the key factors in suppressing Ostwald ripening in foams and emulsions, thereby contributing to the formation of stable dispersions.[75,76] At low surface pressures ($\pi <$ 5 mN m^{-1}), E_G increased similarly at pH = 3 and pH = 9. However, at higher surface pressures, E_G values were consistently greater at pH = 9, suggesting that microgel arrays formed under basic conditions are mechanically more robust. This trend is consistent with previous findings for other pNIPAm-based microgels at fluid interfaces,[54] indicating that electrostatic interactions enhance interfacial elasticity. Regarding this difference, Schmitt *et al.* have recently reported a clear correlation between the influence of charge on the mechanical response of monolayer films and its impact on two-dimensional phase behavior at oil/water interfaces.[53] Although previous studies have examined interfacial compression and elasticity, direct visualization of the structural changes under different pH conditions has remained limited. The authors demonstrated that, at low compression, charged microgels are more easily compressed owing to their smaller effective surface area at the liquid–liquid interface. Under high compression, however, the compressibility is governed by out-of-plane interactions arising from particle swelling, reversing the trend observed in the low-surface-pressure regime and resulting in higher film elasticity. In this study, in order to enable the direct visualization of significant pH-responsive behavior of microgels at the air/water interface, we used microgels with a high amount of acrylic acid (AAc, ~30 mol%) and a low amount of crosslinker (BIS, ~1 mol%) that were fed during the polymerization process. Consequently, the shape of the π–A isotherms differed substantially from those reported previously, and the surface-compression modulus exhibited a marked dependence on the microgel-charge state. Notably, at high compression, deprotonated microgels displayed a higher compression modulus than the other samples, suggesting that their compression may involve a similar out-of-plane interaction mechanism as proposed by Schmitt *et al.* While such three-dimensional interparticle interactions likely contribute to the

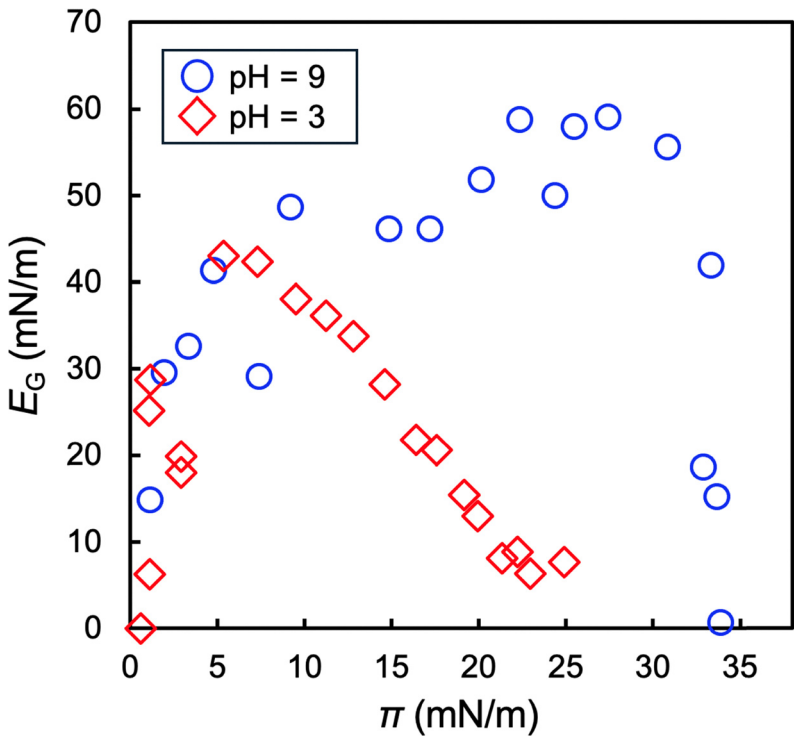

Fig. 7 Surface elasticity, $E_G = -d\pi/d \ln A$, as a function of surface pressure for microgels at pH = 3 (red diamonds) and pH = 9 (blue circles).

observed behavior, our results indicate that the decrease in interparticle distance at high compression occurs independently of charge state. However, only at pH = 3 did the degree of ordering deteriorate. These findings suggest that the electrostatic repulsion between microgels and the maintenance of in-plane ordering may play a crucial role in determining the mechanical properties of soft microgel arrays.

In summary, this study thus bridges the gap between structural and mechanical perspectives in understanding microgel monolayers at fluid interface, where the state changes in response to external stimuli. Microgels containing a large amount of pH-responsive polymers are strongly affected by the pH value of the aqueous phase, even at the air/water interface, resulting in significant differences in the array structures and compression modulus of the microgel arrays. Highly charged microgels form highly ordered structures at the air/water interface and exhibit strong resistance to lateral compression. In order to clarify and more systematically understand the influence of the external environment on the compression behavior of microgels at the air/water interface, it is essential to combine advanced imaging techniques such as neutron reflectivity,[77] small-angle light scattering (SALS),[78] and atomic-force microscopy (AFM)[49,50] in order to elucidate the three-dimensional structure of deformed microgels at interfaces. However, our findings not only enhance the fundamental understanding of microgel-compression behavior at fluid interfaces but also open new avenues for the design of stimuli-responsive materials for applications in foams and emulsions, as well as for the nano/microstructural engineering of soft, deformable particles in two- and three-dimensional configurations.

Conclusions

In this study, we have quantitatively evaluated the pH-dependent compression behavior of poly(NIPAm-*co*-AAc) microgels at the air/water interface using direct visualization and surface-pressure measurements. At pH = 3, the microgels are weakly charged and form disordered monolayers due to reduced electrostatic repulsion. In contrast, at pH = 9, the microgels are highly swollen and strongly charged, resulting in the formation of highly ordered hexagonal arrays with high colloidal crystallinity. Notably, when the subphase pH was lowered after forming ordered arrays at pH = 9, the microgels retained their highly ordered positions, suggesting that the ordered arrays nearly completely covered the interface, thereby restricting particle movement and allowing slight entanglement of polymer chains between neighboring microgels. Furthermore, surface-compression-modulus measurements revealed significantly higher interfacial elasticity at pH = 9, which correlates with the observed ordering of microgels. These results demonstrate that pH-dependent variations in electrostatic charge and swelling profoundly influence the interfacial ordering and mechanical response of microgels at the air/water interface. Such insights offer practical design principles for the development of stimuli-responsive soft materials and for enhancing the stability of foams and emulsions.

Author contributions

T. K. wrote the draft of the manuscript. H. M. and D. S. revised the manuscript. T. K. synthesized the microgels, conducted a series of evaluations of microgels, and assessed the compression behavior of the microgels at the air/water interface using the LB trough. H. M. participated in discussions related to the entire paper. D. S. designed and supervised the overall study.

Conflicts of interest

There are no conflicts to declare.

Data availability

The data supporting the findings of this study are available in the supplementary information (SI). Supplementary information contains detailed experimental data and additional figures. See DOI: **https://doi.org/10.1039/d5sm00892a**.

Acknowledgements

D. S. gratefully acknowledges a CREST grant-in-aid (JPMJCR21L2) from the Japan Science and Technology Agency (JST), the Iketani Science & Technology Foundation (0351083-A), and a Grant-in-Aid for Challenging Exploratory Research (24K21792). H. M. gratefully acknowledges a Grant-in-Aid for Scientific Research (C) (25K08744) from the Japan Society for the Promotion of Science (JSPS). This work was also supported by JST SPRING, Japan under grant number JPMJSP2126.

Notes and references

1 R. Pelton, *Adv. Colloid Interface Sci.*, 2000, **85**, 1.
2 S. Nayak and L. A. Lyon, *Angew. Chem., Int. Ed.*, 2005, **44**, 7686.
3 F. A. Plamper and W. Richtering, *Acc. Chem. Res.*, 2017, **50**, 131.
4 D. Suzuki, K. Horigome, T. Kureha, S. Matsui and T. Watanabe, *Polym. J.*, 2017, **49**, 695.
5 M. Karg, A. Pich, T. Hellweg, T. Hoare, L. A. Lyon, J. J. Crassous, D. Suzuki, R. A. Gumerov, S. Schneider, I. I. Potemkin and W. Richtering, *Langmuir*, 2019, **35**, 6231.
6 Y. Nishizawa, K. Honda and D. Suzuki, *Chem. Lett.*, 2021, **50**, 1226.
7 Y. Hoshino, K. Imamura, M. Yue, G. Inoue and Y. Miura, *J. Am. Chem. Soc.*, 2012, **134**, 18177.
8 H. Kawaguchi, *Polym. Int.*, 2014, **63**, 925.
9 T. Kureha, Y. Nishizawa and D. Suzuki, *ACS Omega*, 2017, **2**, 7686.
10 T. Kureha and D. Suzuki, *Langmuir*, 2018, **34**, 837.
11 S. Matsui, K. Hosho, H. Minato, T. Uchihashi and D. Suzuki, *Chem. Commun.*, 2019, **55**, 10064.
12 C. C. Cutright, J. L. Harris, S. Ramesh, S. A. Khan, J. Genzer and S. Menegatti, *Adv. Funct. Mater.*, 2021, **31**, 2104164.
13 M. Ballauff and Y. Lu, *Polymer*, 2007, **48**, 1815.
14 T. Kureha, Y. Nagase and D. Suzuki, *ACS Omega*, 2018, **3**, 6158.

15 V. Sabadasch, M. Dirksen, P. Fandrich, J. Cremer, N. Biere, D. Anselmetti and T. Hellweg, *ACS Appl. Mater. Interfaces*, 2022, **14**, 49181.
16 T. Kharandiuk, K. H. Tan, I. Kubiska, M. A. A. Enezy-Ulbrich, V. Ivasiv, R. Nebesnyi, I. I. Potemkin and A. Pich, *React. Chem. Eng.*, 2022, **7**, 2192.
17 T. Hellweg, C. D. Dewhurst, E. Bruckner, K. Kratz and W. Eimer, *Colloid Polym. Sci.*, 2000, **278**, 972.
18 L. A. Lyon, J. D. Debord, S. B. Debord, C. D. Jones, J. G. McGrath and M. J. Serpe, *J. Phys. Chem. B*, 2004, **108**, 19099.
19 D. Suzuki, J. G. McGrath, H. Kawaguchi and L. A. Lyon, *J. Phys. Chem. C*, 2007, **111**, 5667.
20 J. Mattsson, H. M. Wyss, A. Fernandez-Nieves, K. Miyazaki, Z. Hu, D. R. Reichman and D. A. Weitz, *Nature*, 2009, **462**, 83.
21 D. Suzuki, T. Yamagata, K. Horigome, K. Shibata, A. Tsuchida and T. Okubo, *Colloid Polym. Sci.*, 2012, **290**, 107.
22 S. Minami, D. Suzuki and K. Urayama, *Curr. Opin. Colloid Interface Sci.*, 2019, **43**, 113.
23 S. Saxena, C. E. Hansen and L. A. Lyon, *Acc. Chem. Res.*, 2014, **47**, 2426.
24 A. C. Brown, S. E. Stabenfeldt, B. Ahn, R. T. Hannan, K. S. Dhada, E. S. Herman, V. Stefanelli, N. Guzzetta, A. Alexeev, W. A. Lam, L. A. Lyon and T. H. Barker, *Nat. Mater.*, 2014, **13**, 1108.
25 D. Suzuki, T. Sakai and R. Yoshida, *Angew. Chem., Int. Ed.*, 2008, **47**, 917.
26 D. Suzuki, H. Taniguchi and R. Yoshida, *J. Am. Chem. Soc.*, 2009, **131**, 12058.
27 D. Suzuki, T. Kobayashi, R. Yoshida and T. Hirai, *Soft Matter*, 2012, **8**, 11447.
28 S. Matsui, K. Inui, Y. Kumai, R. Yoshida and D. Suzuki, *ACS Biomater. Sci. Eng.*, 2019, **5**, 5615.
29 K. Inui, I. Saito, R. Yoshida, H. Minato and D. Suzuki, *ACS Appl. Polym. Mater.*, 2021, **3**, 3298.
30 X. Guan, H. Jiang, J. Lin and T. Ngai, *Curr. Opin. Colloid Interface Sci.*, 2024, **73**, 101827.
31 L. Braun, M. Kuhnhammer and R. V. Klitzing, *Curr. Opin. Colloid Interface Sci*, 2020, **50**, 101379.
32 T. Watanabe, M. Takizawa, H. Jiang, T. Ngai and D. Suzuki, *Chem. Commun.*, 2019, **55**, 5990.
33 Y. Nishizawa, T. Watanabe, T. Noguchi, M. Takizawa, C. Song, K. Murata, H. Minato and D. Suzuki, *Chem. Commun.*, 2022, **58**, 12927.
34 M. Rey, M. A. Fernandez-Rodriguez, M. Karg, L. Isa and N. Vogel, *Acc. Chem. Res.*, 2020, **53**, 414.
35 D. Feller and M. Karg, *Soft Matter*, 2022, **18**, 6301.
36 W. Richtering, *Langmuir*, 2012, **28**, 17218.
37 M. A. Fernandez-Rodriguez, A. Martín-Molina and J. Maldonado-Valderrama, *Adv. Colloid Interface Sci.*, 2021, **288**, 102350.
38 S. Stock and R. V. Klitzing, *Curr. Opin. Colloid Interface Sci.*, 2022, **58**, 101561.
39 R. H. Pelton and P. Chibante, *Colloids Surf.*, 1986, **20**, 247.
40 Y. Nishizawa, S. Matsui, K. Urayama, T. Kureha, M. Shibayama, T. Uchihashi and D. Suzuki, *Angew. Chem., Int. Ed.*, 2019, **58**, 8809.
41 J. Zhang and R. Pelton, *Langmuir*, 1999, **15**, 8032.
42 H. Minato, M. Murai, T. Watanabe, S. Matsui, M. Takizawa, T. Kureha and D. Suzuki, *Chem. Commun.*, 2018, **54**, 932.
43 M. Destribats, V. Lapeyre, M. Wolfs, E. Sellier, F. Leal-Calderon, V. Ravaine and V. Schmitt, *Soft Matter*, 2011, **7**, 7689.
44 M.-H. Kwok and T. Ngai, *J. Colloid Interface Sci.*, 2016, **461**, 409.
45 N. V. Bushuev, R. A. Gumerov, S. Bochenek, A. Pich, W. Richtering and I. I. Potemkin, *ACS Appl. Mater. Interfaces*, 2020, **12**, 19903.
46 S. Bochenek, F. Camerin, E. Zaccarelli, A. Maestro, M. M. Schmidt, W. Richtering and A. Scotti, *Nat. Commun.*, 2022, **13**, 3744.
47 A. Rubio-Andrés, D. Bastos-González and M. A. Fernandez-Rodriguez, *J. Colloid Interface Sci.*, 2025, **688**(15), 328.
48 F. Grillo, M. A. Fernandez-Rodriguez, M. Antonopoulou, D. Gerber and L. Isa, *Nature*, 2020, **582**, 219.
49 J. Vialetto, S. N. Ramakrishna and L. Isa, *Sci. Adv.*, 2022, **8**, 45.
50 J. Vialetto, F. Camerin, S. N. Ramakrishna, E. Zaccarelli and L. Isa, *Adv. Sci.*, 2023, **10**, 2303404.
51 M. Rey, X. Hou, J. S. J. Tang and N. Vogel, *Soft Matter*, 2017, **13**, 8717.
52 Y. Yang, J. Maldonado-Valderrama and A. Martín-Molina, *J. Mol. Liq.*, 2020, **303**, 112678.
53 M. M. Schmidt, S. Bochenek, A. A. Gavrilov, I. I. Potemkin and W. Richtering, *Langmuir*, 2020, **36**, 11079.
54 M. M. Schmidt, O. Laukkanen, S. Bochenek, W. S. Schier and W. Richtering, *J. Rheol.*, 2024, **68**, 553.
55 M. Rey, J. Kolker, J. A. Richards, I. Malhotra, T. S. Glen, N. Y. D. Li, F. H. J. Laidlaw, D. Renggli, J. Vermant, A. B. Schofield, S. Fujii, H. Löwen and P. S. Clegg, *Nat. Commun.*, 2023, **14**, 6723.
56 M. M. Schmidt, J. Ruiz-Franco, S. Bochenek, F. Camerin, E. Zaccarelli and A. Scotti, *Phys. Rev. Lett.*, 2023, **131**, 258202.
57 S. Huang, K. Gawlitza, R. von Klitzing, W. Steffen and G. K. Auernhammer, *Macromolecules*, 2017, **50**, 3680.
58 F. Camerin, N. Gnan, J. Ruiz-Franco, A. Ninarello, L. Rovigatti and E. Zaccarelli, *Phys. Rev. X*, 2020, **10**, 031012.
59 W. Liu, Z. Zhao, L. Zhang, K. Zhou, P. W. F. Yeung, H. Jiang, C. Yang, Y. Zhu and T. Ngai, *ACS Macro Lett.*, 2025, **14**, 564.
60 K. Horigome and D. Suzuki, *Langmuir*, 2012, **28**, 12962.
61 D. Suzuki and K. Horigome, *J. Phys. Chem. B*, 2013, **117**, 9073.
62 M. Takizawa, Y. Sazuka, K. Horigome, Y. Sakurai, S. Matsui, H. Minato, T. Kureha and D. Suzuki, *Langmuir*, 2018, **34**, 4515.
63 H. Minato, M. Takizawa, S. Hiroshige and D. Suzuki, *Langmuir*, 2019, **35**, 10412.
64 K. Honda, Y. Sazuka, K. Iizuka, S. Matsui, T. Uchihashi, T. Kureha, M. Shibayama, T. Watanabe and D. Suzuki, *Angew. Chem., Int. Ed.*, 2019, **58**, 7294.
65 Y. Sasaki, S. Hiroshige, M. Takizawa, Y. Nishizawa, T. Uchihashi, H. Minato and D. Suzuki, *RSC Adv.*, 2021, **11**, 14562.
66 H. Minato, Y. Sasaki, K. Honda, T. Watanabe and D. Suzuki, *Adv. Mater. Interfaces*, 2022, **9**, 2200879.
67 D. Suzuki, *Langmuir*, 2023, **39**, 7525.

68 T. Kawamoto, K. Yanagi, Y. Nishizawa, H. Minato and D. Suzuki, *Chem. Commun.*, 2023, **59**, 13289.
69 Y. Sasaki, Y. Nishizawa, N. Watanabe, T. Uchihashi and D. Suzuki, *Macromol. Rapid Commun.*, 2024, **46**, 2400604.
70 T. Kawamoto, H. Minato and D. Suzuki, *Soft Matter*, 2024, **20**, 5836.
71 K. Urayama, T. Saeki, S. Cong, S. Uratani, T. Takigawa, M. Murai and D. Suzuki, *Soft Matter*, 2014, **10**, 9486.
72 F. Pinaud, K. Geisel, P. Masse, B. Catargi, L. Isa, W. Richtering and V. Schmitt, *Soft Matter*, 2014, **10**, 6963.
73 C. Picard, P. Garrigue, M. C. Tatry, V. Lapeyre, S. Ravaine, V. Schmitt and V. Ravaine, *Langmuir*, 2017, **33**, 7968.
74 M. Rey, M. Á. Fernández-Rodríguez, M. Steinacher, L. Scheidegger, K. Geisel, W. Richtering, T. M. Squires and L. Isa, *Soft Matter*, 2016, **12**, 3545.
75 M. B. J. Meinders and T. van Vliet, *Adv. Colloid Interface Sci.*, 2004, **108**, 119.
76 D. Georgieva, A. Cagna and D. Langevin, *Soft Matter*, 2009, **5**, 2063.
77 Y. Gerelli, F. Camerin, S. Bochenek, M. M. Schmidt, A. Maestro, W. Richtering, E. Zaccarelli and A. Scotti, *Soft Matter*, 2024, **20**, 3653.
78 K. Kuk, V. Abgarjan, L. Gregel, Y. Zhou, V. C. Fadanelli, I. Buttinoni and M. Karg, *Soft Matter*, 2023, **19**, 175.